ORGANIC ELECTRONICS

Increasing the dimensionality of transistors with hydrogels

Dingyao Liu[1]†, Jing Bai[1]†, Xinyu Tian[1]†, Yan Wang[1]†, Binbin Cui[1], Shilei Dai[1], Wensheng Lin[1], Zhuowen Shen[2], Chun Kit Lai[2], George G. Malliaras[3]*, Shiming Zhang[1,2]*

Transistors, fundamental to modern electronics, are traditionally rigid, planar, and two-dimensional (2D), limiting their integration with the soft, irregular, and three-dimensional (3D) nature of biological systems. Here, we report 3D semiconductors, integrating organic electronics, soft matter, and electrochemistry. These 3D semiconductors, in the form of hydrogels, realize millimeter-scale modulation thickness while achieving tissue-like softness and biocompatibility. This breakthrough in modulation thickness is enabled by a templated double-network hydrogel system, where a secondary porous hydrogel guides the 3D assembly of a primary redox-active conducting hydrogel. We demonstrate that these 3D semiconductors enable the exclusive fabrication of 3D spatially interpenetrated transistors that mimic real neuronal connections. This work bridges the gap between 2D electronics and 3D living systems, paving the way for advanced bioelectronics systems such as biohybrid sensing and neuromorphic computing.

Transistors are the fundamental building blocks of modern electronic devices (*1*), driving advancements in computing performance by becoming smaller, faster, and more integrated. However, as transistor miniaturization approaches physical and technological limits, as predicted by Moore's law, traditional designs are increasingly constrained (*2*–*4*).

At the same time, emerging fields such as bioelectronics are exploring new paradigms that integrate electronics with living biological systems to enable transformative applications (*5*–*7*), including biohybrid sensing and neuromorphic computing (*8*–*10*). These systems promise low-power operation, high efficiency, and new functionality, but achieving seamless integration between electronics and biology remains a challenge. The core issue lies in the fundamental mismatches between conventional transistors and biological systems. Traditional transistors are rigid, planar, and inherently two-dimensional (2D) (*11*), whereas biological systems are soft, irregular, and three-dimensional (3D) (*12*). These differences make it difficult for traditional electronic components to interact effectively with biological tissues, such as neurons, which require 3D spatial integration (*13*). To address this mismatch, new materials and device architectures capable of operating in three dimensions are needed.

Hydrogels have recently emerged as promising materials for bioelectronics owing to their tissue-like properties (*14*–*16*), including biocompatibility, softness, and 3D nature. Recent advances in redox-active hydrogels have further equipped these materials with semiconducting capabilities (*17*), enabling them to serve as active electronic components in transistors (*18*–*20*). Despite these advancements, hydrogel semiconductors remain limited in their ability to modulate conductivity at larger scales. Current technologies are constrained to nano- to micrometer-thick hydrogels (*18*, *19*), where ion transport and ion-electron coupling are effective. However, as thickness increases beyond the micrometer scale, these mechanisms weaken considerably, leading to a loss of semiconducting functionality. Overcoming the thickness limitation is critical to unlocking the full 3D potential of hydrogel semiconductors to enable their spatial integration with living biological systems.

We overcome the thickness limit of hydrogel semiconductors by designing a double-network hydrogel system synthesized entirely in an aqueous environment. First, a secondary stretchable, porous hydrogel acts as a 3D template to guide the assembly of a primary redox-active conducting hydrogel, enhancing electron transport. Second, the network composition and porosity are controlled to facilitate ion transport. Finally, achieving a balance between ion and electron transport maximizes ion-to-electron conversion efficiency, leading to 3D hydrogel semiconductors with millimeter-scale modulation thickness while maintaining tissue-like properties.

Strategy to enable 3D modulation in 3D hydrogel transistors

The assembled 3D hydrogel transistor is a mixed ion-electron transistor, functioning analogously to organic electrochemical transistors (OECTs) (*21*, *22*). The key difference lies in replacing the thin-film semiconducting channel [poly(3,4-ethylendioxythiophene):poly(styrenesulfonate), PEDOT:PSS] (*23*, *24*) with 3D bulk hydrogels to obtain broad tissue-like properties to facilitate bioelectronic integration (*25*). During operation, ions shuttle through the channel, altering its conductivity. For example, when a positive gate voltage is applied, cations from the electrolyte penetrate into the redox-active hydrogel semiconductor, leading to the reaction: $PEDOT^+:PSS^- + M^+ + e^- \longleftrightarrow PEDOT^0 + PSSM$ (*26*, *27*). A typical feature of this reaction is 3D bulk modulation—wherein ions penetrate the entire channel, tuning its conductivity (Fig. 1A). The 3D bulk modulation was experimentally validated through volumetric capacitance measurements, which showed that channel capacitance increases linearly with channel thickness (*28*–*30*).

When attempting to assemble 3D hydrogel transistors by increasing hydrogel thickness, such as through layer-by-layer stacking, the linear relationship between channel capacitance and channel thickness failed to remain consistent at greater thicknesses. This failure resulted in partial 3D modulation and a poor on/off ratio. The underlying issue stems from the limited ability of ions to diffuse into thicker channels (Fig. 1B and figs. S1 and S2) (*31*). Consequently, additional material strategies are required to develop 3D hydrogel semiconductors without compromising their semiconducting properties.

Development of 3D hydrogel semiconductors

To achieve complete 3D modulation in 3D hydrogel semiconductors, the following strategies are used: (i) phase engineering to create a continuous electron transport pathway on the semiconducting backbone (Fig. 2); (ii) structural engineering to optimize hydrogel porosity, facilitating ion transport in the 3D bulk (Fig. 3); and (iii) efficient ion-electron coupling, achieved by the synergy of the above two processes. The process flow in fabricating the hydrogel semiconductor is detailed in the materials and methods in the supplementary materials.

Phase engineering of 3D hydrogel semiconductors

Three phases can exist in a hydrogel semiconductor: water, gel, and a water-gel mixture. For hydrogel semiconductors, achieving a pure gel phase is essential to ensure optimal performance and stability (Fig. 2, A to C). Various methods can be used to evaluate the phase composition (*32*). In the case of PEDOT:PSS hydrogels, the term "reduced viscosity" can be used to characterize the gel-forming process (*33*). An increase in reduced viscosity with higher PEDOT:PSS content is a strong indicator favoring gel formation. To ensure a pure gel phase, the storage modulus should also be substantially larger than the loss modulus. Additionally, under controlled conditions, no water separation or loss should be observed.

[1]Department of Electrical and Electronic Engineering, The University of Hong Kong, Pokfulam, Hong Kong SAR, China. [2]School of Biomedical Engineering, The University of Hong Kong, Pokfulam, Hong Kong SAR, China. [3]Electrical Engineering Division, Department of Engineering, The University of Cambridge, Cambridge, UK. ***Corresponding author. Email: beszhang@hku.hk (S.Z.); gm603@cam.ac.uk (G.G.M.)** †These authors contributed equally to this work.

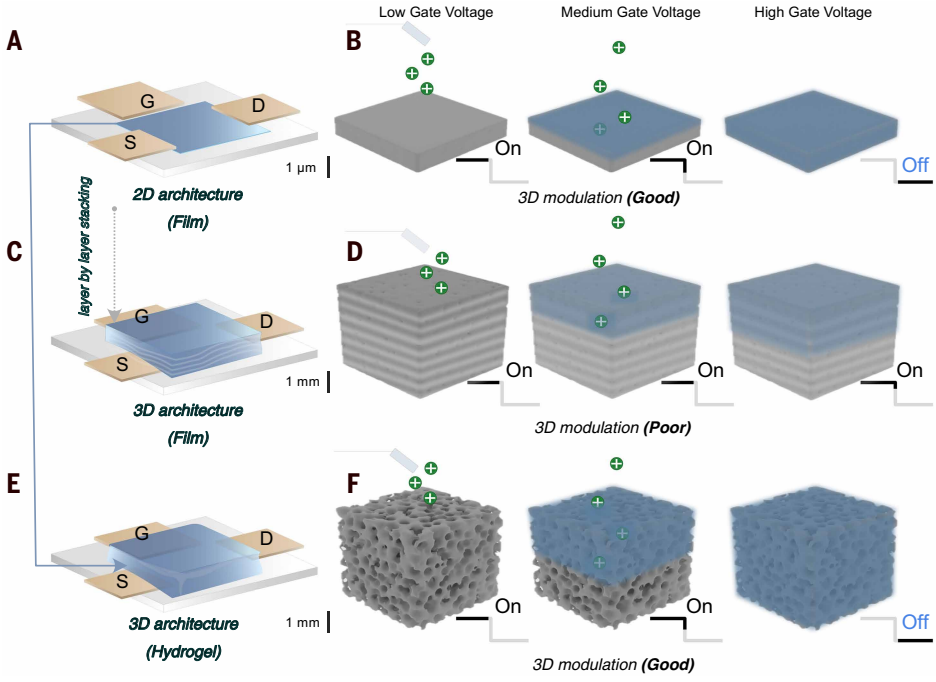

Fig. 1. Strategy to enable 3D modulation in 3D hydrogel transistors. (**A** and **B**) Thin-film OECTs can achieve 3D modulation but are limited to a 2D architecture (with channel thickness ranging between nanometers and micrometers). S, source; G, gate; D, drain. (**C** and **D**) A 3D architecture can be created by directly increasing the channel thickness, but this results in insufficient 3D modulation owing to compromised ion diffusion. (**E** and **F**) Hydrogel semiconductors, through precise phase and structural control, enable efficient 3D modulation in a 3D transistor, achieved by balancing ion and electron transport within the hydrogel.

It is also essential to form a continuous $PEDOT^+$ phase within the hydrogel semiconductor to facilitate electron transport (*34*). For a pure PEDOT:PSS hydrogel semiconductor, the semiconducting polymer network is often discontinuous because of the blockage caused by nonconducting networks, resulting in limited semiconducting properties (Fig. 2D and fig. S3).

We found that phase continuity, and consequently the long-range π-π ordering essential for semiconducting properties, can be controlled by the secondary hydrogel network. (Fig. 2, D to G). For example, combining PEDOT:PSS hydrogels with polyethylene glycol diacrylate (PEGDA), polyvinyl alcohol (PVA), polyacrylamide (PAAm), or polyacrylic acid (PAA) led to increased conductivity from 0.9 S/cm to 1.4, 18, and 100 S/cm, respectively (Fig. 2E), indicating enhanced continuity of the conductive $PEDOT^+$ phase (figs. S4 to S6). These results align with previous reports on the development of conducting hydrogels (*34*–*37*), which have revealed that secondary networks, especially PAA, can serve as efficient templates to guide the formation of continuous $PEDOT^+$ monolayers (*34*, *38*). The increased conductivity is also associated with improved volume capacitance (Fig. 2F and fig. S7), a strong indicator of the formation of a 3D electron-conducting network. The improved phase continuity also does not compromise the mechanical properties of the hydrogel semiconductor (Fig. 2G and figs. S8 to S11).

Structure engineering of 3D hydrogel semiconductors

To achieve 3D modulation at greater thicknesses, such as up to the millimeter scale, requires additional structural design to control porosity that enhances ion transport (*32*). The structure engineering is crucial for enabling efficient ion-electron conversion within 3D hydrogel semiconductors. To tune the porosity of the hydrogel semiconductor, we used the following strategies: (i) controlling the individual concentrations of components in the mixture that assembles the multinetwork hydrogel, including the primary semiconducting network and the secondary stretchable network; (ii) adjusting the cross-linking density by varying the concentration of the cross-linker; and (iii) using solvent exchange to deliberately construct micropores after hydrogel formation (detailed in the materials and methods). The combination of these approaches delivers a hydrogel semiconductor with porosity controllable over a wide range, from 5% to 90% (Fig. 3).

We observed that the porosity of the hydrogel semiconductor is positively correlated with its swelling ratio. For example, the swelling ratio increased from 50% to 100%, and eventually to 500%, as the porosity increased from 5% to 10% and then to 90%. These swelling properties were found to be reversible, demonstrating the mechanical robustness of the microporous structure (Fig. 3, A to C).

To investigate the dependence of charge carrier transport on porosity, we measured both the electronic conductivity and ionic conductivity of the hydrogel semiconductors with varying porosities. We found that increasing the porosity decreases the electronic conductivity but enhances the ionic conductivity. Specifically, increasing the porosity from 5% to 90% resulted in a decrease in electronic conductivity by more than an order of magnitude (Fig. 3D), whereas ionic conductivity increased by more than an order of magnitude (Fig. 3E). This behavior is reasonable and can be explained as follows: Increasing porosity makes the electron-conducting network sparser, thereby reducing electronic conductivity, while simultaneously providing more space for ionic transport, which enhances ionic conductivity.

We observed that an optimal porosity range exists for the 3D hydrogel semiconductor that corresponds to the highest on/off ratio of 10^4, comparable to state-of-the-art OECTs (Fig. 3F) (*39*, *40*). This observation indicates that optimal ion-electron coupling is achieved at this porosity. The results are in line with our steady-state simulation results based on the Bernards-Malliaras model (figs. S12 to S14) (*27*). This phenomenon can be explained as follows: (i) At low porosity, the semiconducting polymer network is dense, which favors electron transport but restricts ion penetration. (ii) At high porosity, the semiconducting polymer network becomes loose, leading to poor electronic transport and limiting ion-electron redox coupling despite enhanced ionic transport.

Validation of 3D modulation in 3D hydrogel semiconductors

To evaluate the degree of 3D modulation in hydrogel semiconductors, we fabricated hydrogel transistors (Fig. 4A and fig. S15). The typical transfer and output curves (Fig. 4, B and C) demonstrate that devices made with a 3D hydrogel semiconductor exhibit superior performance than the reference films of the same channel thicknesses (between 50 and 1000 μm). For instance, at the same thickness of 1 mm—sufficient to sustain a 3D freestanding architecture—the on/off ratio of the hydrogel transistors reaches ~10^4 (Fig. 4), which is three orders of magnitude higher than the reference 1-mm-thick OECTs. This result proves the high doping/dedoping efficiency of the 3D hydrogel semiconductor.

The efficient 3D modulation is further validated by the volumetric capacitance of the hydrogel semiconductor, a standard parameter used to evaluate bulk modulation in OECTs (Fig. 4D). For OECTs fabricated

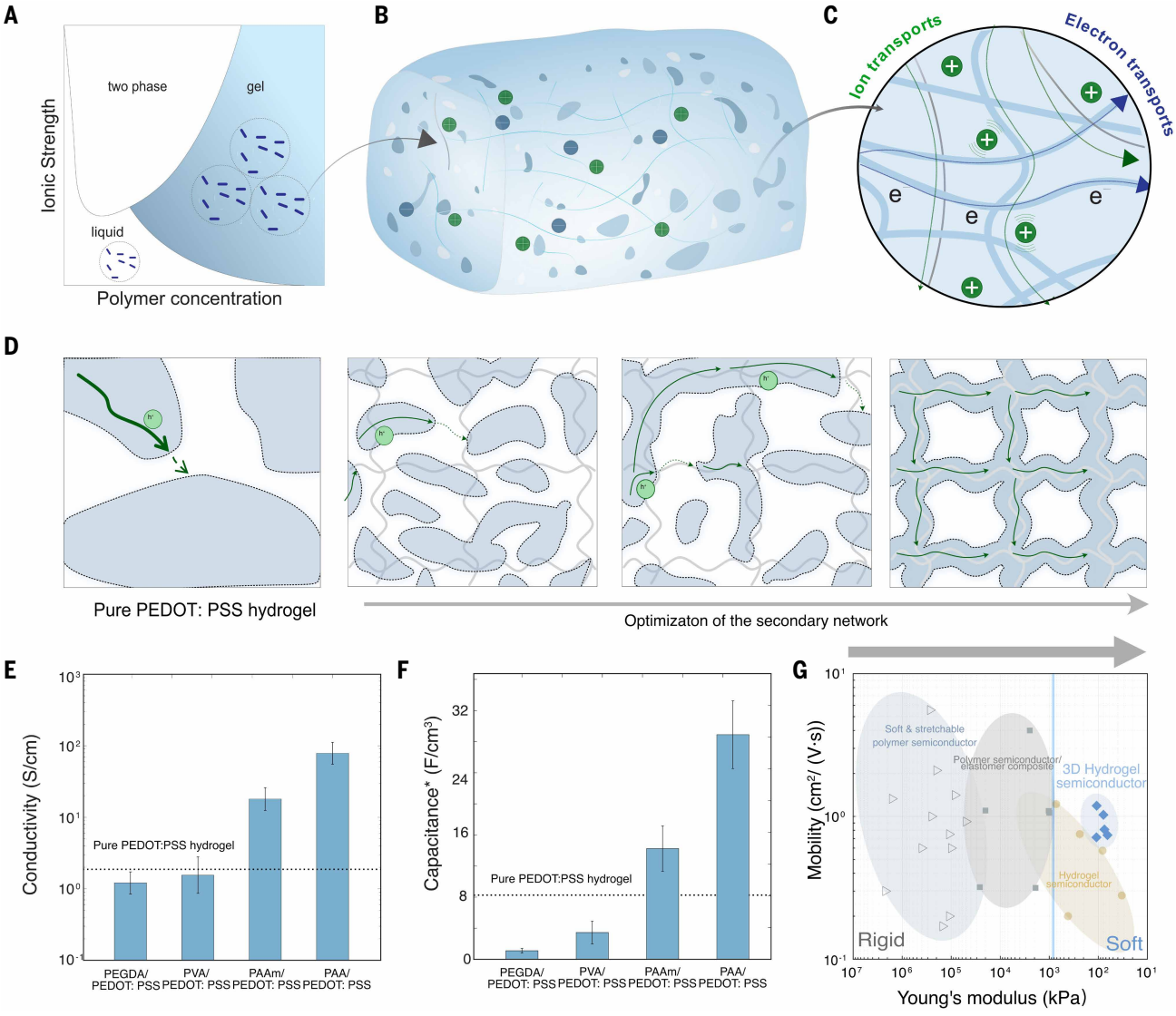

Fig. 2. Phase engineering of 3D hydrogel semiconductors to promote electron transport. (**A** to **C**) A hydrogel may contain three phases: a liquid phase, a gel phase, and a mixture of the two. In a hydrogel semiconductor, mixed conduction pathways exist, including ions and electrons. (**D**) Illustration of phase variations in hydrogel semiconductors (using PEDOT:PSS as the primary semiconducting backbone) by optimizing the secondary hydrogel networks. (**E** and **F**) A comparison of these hydrogel semiconductors shows that a continuous phase favors both high electrical conductivity and high volumetric capacitance. The hydrogel semiconductors include pure PEDOT:PSS hydrogel and double network hydrogel employing polyvinyl alcohol (PVA), polyacrylamide (PAAm), and polyacrylic acid (PAA) as the secondary network. Data are presented as mean ± SD, $N = 3$ independent hydrogel samples per condition. (**G**) The resultant hydrogel semiconductor (PEDOT:PSS/PAA) overcomes the modulus limitations of existing soft semiconductors while maintaining a mobility of ~1 $cm^2/(V \cdot s)$ (table S1).

with conventional thin films, the capacitance fails to increase linearly when the channel thickness exceeds ~10 μm (Fig. 4D), which is in line with previous studies (*31*). In contrast, the linear thickness-capacitance dependency of hydrogel semiconductor remains consistent regardless of thickness (up to millimeters), indicating that complete 3D modulation is achieved in the hydrogel semiconductor.

The parameter combination μC^* (where μ is electronic mobility and C^* is the volumetric charge storage capacity) is regarded as a material figure of merit for OECTs (*41*). To provide a fair comparison with conventional films, we further evaluated the thickness-dependent parameter $d\mu C^*$, where channel thickness (d) must satisfy the thickness-capacitance linearity (*28*, *41*). This parameter is essential, as it directly correlates with the transconductance (G_m) of the hydrogel semiconductor transistors. As shown in Fig. 4E, the $d\mu C^*$ of hydrogel semiconductor reaches 0.1 $F \cdot V^{-1} \cdot s^{-1}$, which is significantly higher than that of conventional OECTs with 2D architecture. This improvement is attributed to the greater channel thickness (up to millimeters), while still retaining linear thickness-capacitance behavior. Consequently, the G_m of the resulting 3D hydrogel transistors surpasses reported 2D counterparts (Fig. 4F).

Scalable production of 3D hydrogel semiconductors

To fully leverage the potential of 3D hydrogel semiconductors for demonstrating 3D transistors, it is essential to enable scalable production using accessible and low-cost methods such as printing and textile manufacturing methods. We developed a one-step water-processable fabrication protocol, detailed in the materials and methods. In this approach, the required materials for assembling the composite

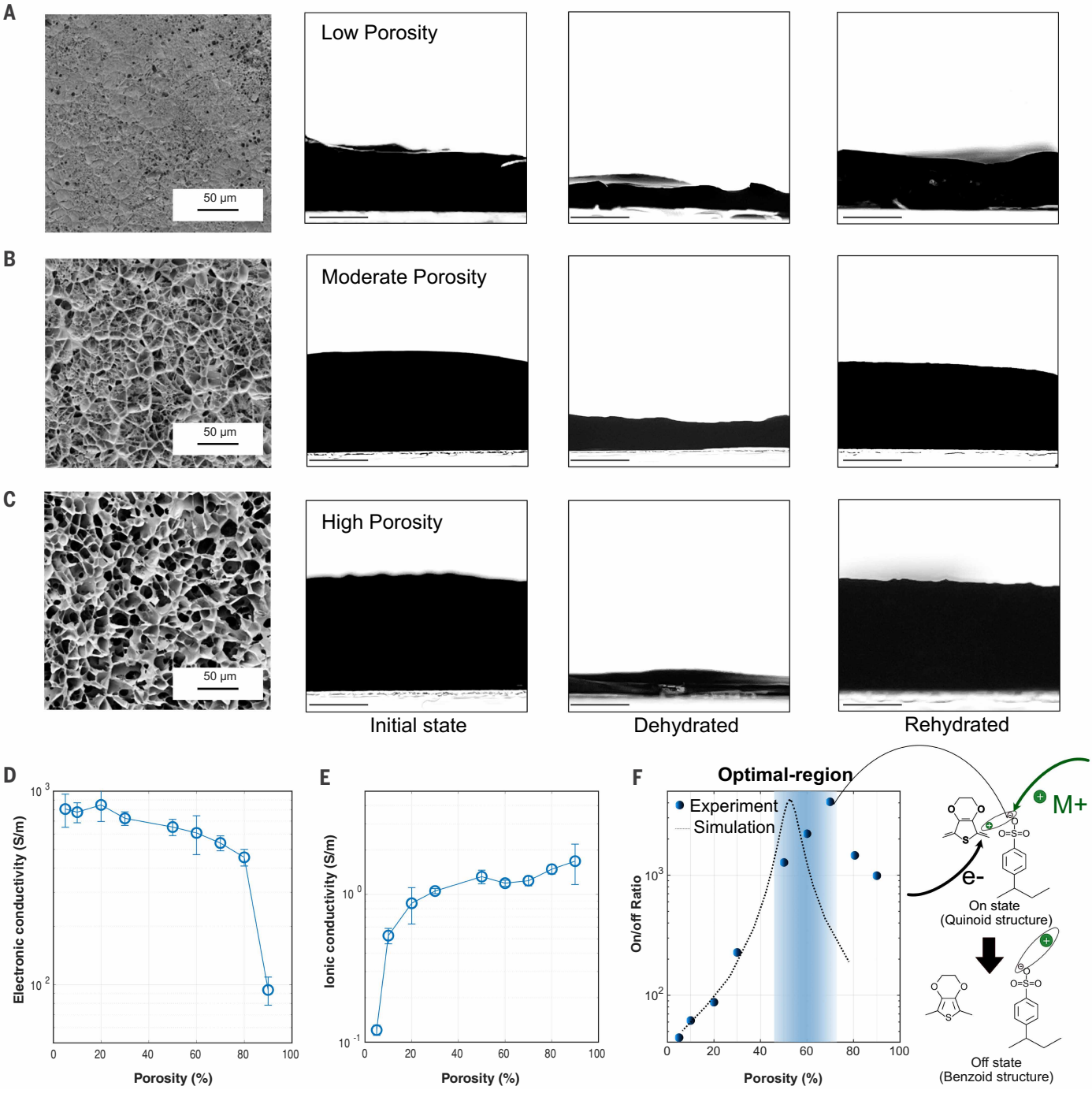

Fig. 3. Structural engineering of 3D hydrogel semiconductors to promote ion transport. (**A** to **C**) Porosity in hydrogel semiconductors (PEDOT:PSS/PAA) can be controlled through solvent exchange and annealing. Cyro–scanning electron microsopy images of hydrogel semiconductors show (A) low porosity (5%), (B) moderate porosity (50%), and (C) high porosity (90%). All hydrogels fully recover their initial volume after dehydration, demonstrating the robustness of the 3D cross-linked network. Scale bars: 500 μm. (**D** and **E**) The increase in porosity decreases electrical conductivity (σ_e) but enhances ionic conductivity (σ_i). Data are presented as mean ± SD, $N = 3$ independent hydrogel samples per condition. (**F**) An optimal porosity range exists (optimal region), corresponding to the highest on/off ratio when characterized with OECT (width of 1 cm, length of 0.5 cm, thickness of 100 μm). These experimental results align with steady-state simulation predictions based on the Bernards-Malliaras model.

hydrogel semiconductor are premixed in a single step. The 3D hydrogel semiconductor can then be formed through a simple cross-linking process. Additional steps can be applied on demand to fine-tune specific parameters. For instance, solvent exchange can be used to adjust porosity.

We mass-produced 3D hydrogel semiconductors with thicknesses ranging from micrometers to millimeters and arbitrary macroscopic shapes (figs. S16 and S17). All these 3D hydrogel semiconductors were examined and found to retain excellent semiconducting properties and mechanical stretchability (Fig. 5A and fig. S18).

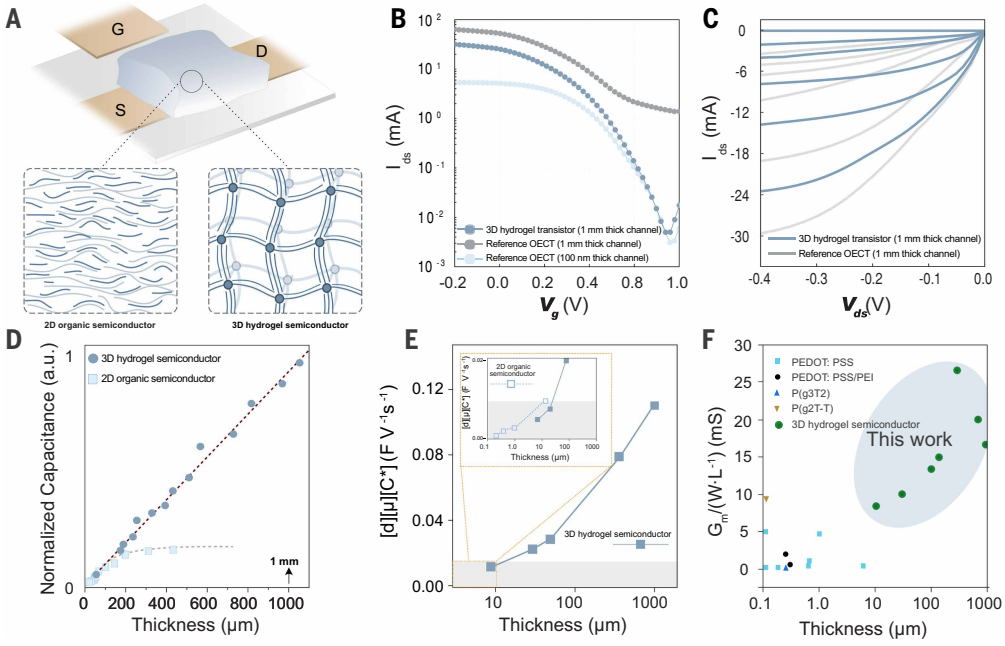

Fig. 4. Electrical performance of 3D hydrogel transistors. (**A**) Comparison of transistors with 2D organic semiconductors (pure PEDOT:PSS film) and 3D hydrogel semiconductors (PEDOT:PSS/PAA) as the channel (with the same thickness of 1 mm). Hydrogel semiconductors, because of their intentionally constructed resilient, three-dimensionally cross-linked micropores, ensure efficient 3D modulation even at greater thicknesses (>50 μm). (**B** and **C**) Comparison of the transfer (V_{ds} = −0.2 V) and output curves (V_g from 0 V to 1 V with 0.2 V increments) of 3D hydrogel transistors (with 1-mm-thick PEDOT:PSS/PAA hydrogel semiconductor as the channel) and reference OECT (with 1 mm and 100 nm PEDOT:PSS film as the channel). The width and length of the device is 1 cm and 0.5 cm, respectively. (**D**) Thickness-capacitance relationship. The 2D organic semiconductor (pure PEDOT:PSS film) fails to maintain linearity at greater thicknesses (~10 μm), whereas the hydrogel semiconductor (PEDOT:PSS/PAA) maintains linearity up to 1000 μm—two orders of magnitude higher. a.u., arbitrary units. (**E**) We fabricated 3D hydrogel transistors with thicknesses ranging from 10 to 1000 μm and reference 2D OECTs with thicknesses ranging from 100 nm to 10 μm. Thicknesses >10 μm for 2D OECTs are not shown, as they failed to achieve complete bulk modulation, meaning they did not maintain a linear thickness-capacitance relationship. In contrast, the volumetric capacitance of the hydrogel semiconductor remains valid at greater thicknesses (up to 1 mm), leading to a significant increase in G_m, which is proportional to $d \times \mu \times C^*$. (**F**) The normalized G_m surpasses previously reported values (table S2).

Building 3D transistors and circuits based on 3D hydrogel semiconductors

The successful development of 3D hydrogel semiconductors, along with the scalable production procedures described above, enables their immediate application in constructing 3D transistors. As a demonstration, we further shaped those 3D semiconductors into self-standing hydrogel fibers, facilitating the construction of brain-inspired 3D neuromorphic circuits, which were assembled into 3D, interpenetrated hydrogel transistor arrays for data computing and analysis (Fig. 5, B and C). To facilitate data acquisition, we integrated the 3D transistors with our recently developed coin-sized readout unit, the Personalized Electronic Reader for Electrochemical Transistors (PERfECT; fig. S19) (*42*–*44*).

To demonstrate the potential of our 3D hydrogel transistor circuits for constructing brain-inspired 3D intelligence, we adopted the reservoir computing (RC) framework—a promising machine learning algorithm known for its minimal computational requirements and ability to operate with small training datasets (*45*, *46*). RC uses neuron-like nonlinear hardware units, a role in which our hydrogel transistors excel (fig. S20). Structurally, hydrogel transistors resemble three-terminal transistors, where the gate electrode functions analogously to the presynapse of a neuron, receiving input ionic signals (*47*). The channel between the source and drain electrodes mimics the postsynapse, responding to the gate signals. Operationally, signals at the gate electrode propagate through nonlinear ionic transport via the electrolyte, modulating the channel conductance through a nonlinear electrochemical doping/dedoping process (*48*).

The detailed implementation of our 3D hydrogel transistor circuits in a RC network is illustrated in Fig. 5D. For demonstration purposes, handwritten digit recognition from the Modified National Institute of Standards and Technology (MNIST) dataset was selected as the application (fig. S21) (*49*). The steps include: (i) Input: Preprocessed image signals serve as input to the gate terminal of the 3D hydrogel transistors. All 16 hydrogel fiber semiconductors share a common gate electrode located at the bottom. (ii) Encoding: The 3D hydrogel transistor circuits encode the digital input signals into distinguishable analog signals, thanks to their nonlinear dynamic response behaviors (Fig. 5E). (iii) Analysis: The entire integrated system processes the input image signal sequence by implementing RC and generating predicted results through a hardware-software coprocessing approach. In this setup, the hardware component (hydrogel transistor array) performs the RC, while the software component handles linear readout and classification. During programming, the modulation of a specific volatile transistor originates from both the common gate and the influence of the weighted equivalent gate voltage from all other channels (Fig. 5B). This intentional design mimics the spatial connectivity of real neural networks, forming the foundation of the hydrogel reservoir layer for RC. Figure 5F presents the confusion matrices showing that the system can achieve a prediction accuracy of up to 91.93%, which is comparable to conventional artificial neural networks (*50*). Each matrix is dominated by its diagonal elements, indicating high class-wise accuracy across all digits. Notably, the prediction accuracy can be maintained under up to 30% strain applied in any direction (Fig. 5G).

Our reported 3D hydrogel semiconductors and transistors achieve millimeter-scale 3D modulation with performance comparable to their thin-film counterparts. These advances are enabled by a standardized water-processable synthesis process that precisely controls phase, porosity, and charge transport properties in three dimensions. Our macroscopic fabrication approach allows the mass production of 3D hydrogel semiconductors and transistors in various 3D shapes, overcoming the dimension limitations of 2D planar electronics, as demonstrated in neuromorphic computing circuits.

Leveraging inherent tissue-like properties such as biocompatibility, stretchability, and permeability, these 3D hydrogel semiconductors and transistors bridge the multidimensional gaps between electronics and living systems, enabling robust and durable 3D interfacing. As an example, we further demonstrate that these 3D semiconductors and transistors enable two-way biology-transistor interactions, including

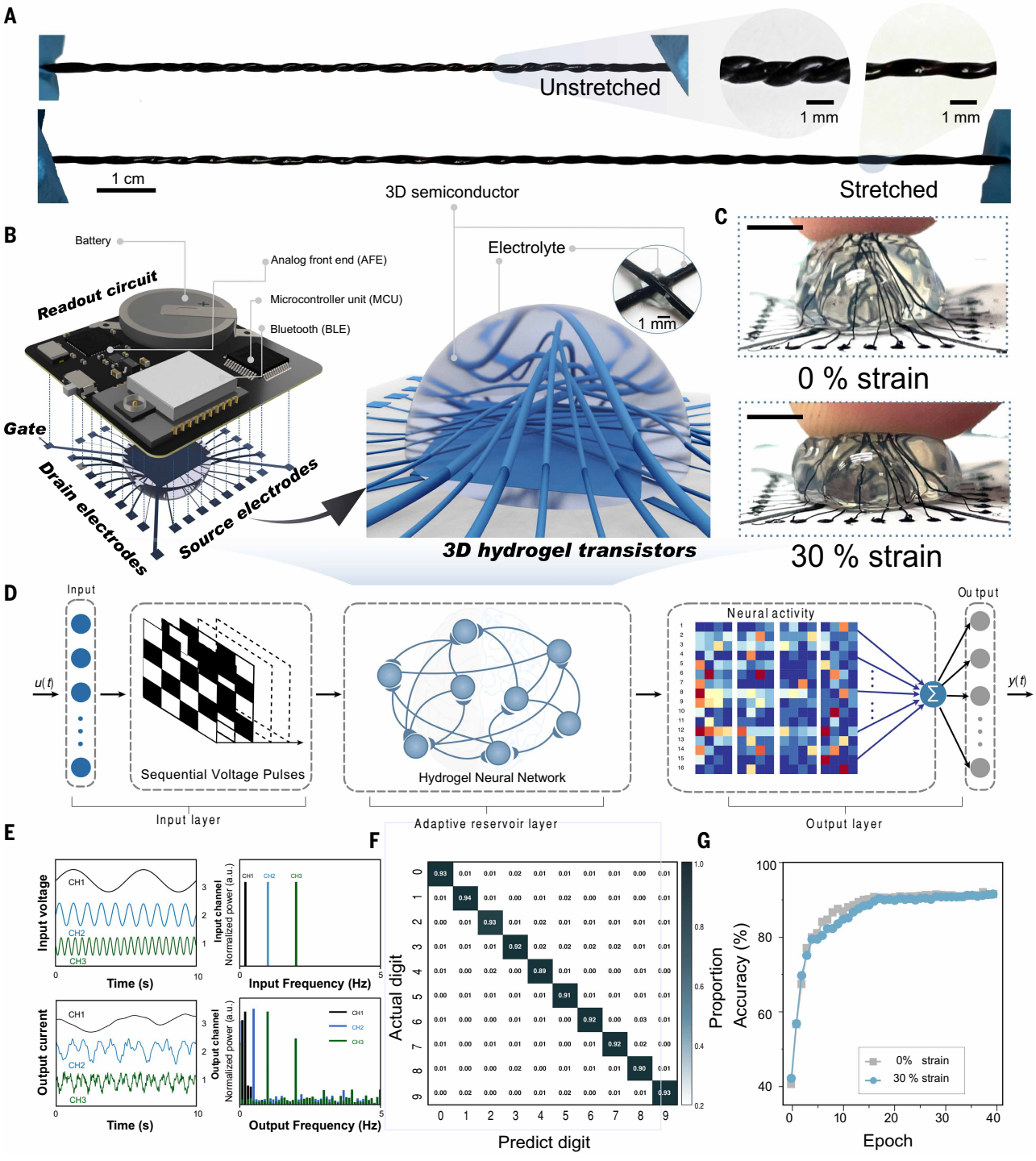

Fig. 5. Increasing the dimensionality of transistors with 3D hydrogel semiconductors. (**A**) The hydrogel semiconductor (PEDOT:PSS/PAA), when fabricated into fiber forms, enables the direct fabrication of 3D, freestanding transistors. (**B**) Illustration of a 3D integrated neuromorphic circuit with the 3D hydrogel transistors. (**C**) Real images of 3D, interpenetrated hydrogel transistors, showing their exclusive ability to resemble the spatial 3D structure of neural circuits in the brain, subjected to strain values of 0% and 30%. Scale bars: 0.5 cm. (**D**) Schematic representation of a 3D RC framework constructed using a 3D hydrogel transistor array. (**E**) Harmonic analysis showing the good nonlinearity of the hydrogel transistors, ensuring high computational efficiency within the reservoir network. (**F**) A confusion matrix showing that handwritten digits are correctly recognized with the hydrogel transistors RC hardware with an accuracy of 91.93%. (**G**) Evolution of prediction accuracy over training epochs when the RC hardware is subjected to strains of 0% and 30%.

cell culture, organoid formation, and programmable cell behavior (fig. S22).

REFERENCES AND NOTES

1. W. Cao *et al.*, *Nature* **620**, 501–515 (2023).
2. C. E. Leiserson *et al.*, *Science* **368**, eaam9744 (2020).
3. J. Shalf, *Philos. Trans. R. Soc. London Ser. A* **378**, 20190061 (2020).
4. I. L. Markov, *Nature* **512**, 147–154 (2014).
5. P. Gkoupidenis *et al.*, *Nat. Rev. Mater.* **9**, 134–149 (2024).
6. A. Carnicer-Lombarte, G. G. Malliaras, D. G. Barone, *Adv. Mater.* **37**, e2408308 (2025).
7. D. Boufidis, R. Garg, E. Angelopoulos, D. K. Cullen, F. Vitale, *Nat. Commun.* **16**, 1861 (2025).
8. Y. Wu *et al.*, *Nat. Commun.* **15**, 4047 (2024).
9. H. Cai *et al.*, *Nat. Electron.* **6**, 1032–1039 (2023).
10. C. Pitsalidis *et al.*, *Sci. Adv.* **4**, eaat4253 (2018).
11. S. D. Brotherton, *Introduction to Thin Film Transistors: Physics and Technology of TFTs* (Springer, 2013).
12. X. Liu, S. Wang, *Chem. Soc. Rev.* **43**, 2385–2401 (2014).
13. T. Schrödel, R. Prevedel, K. Aumayr, M. Zimmer, A. Vaziri, *Nat. Methods* **10**, 1013–1020 (2013).
14. H. Yuk, J. Wu, X. Zhao, *Nat. Rev. Mater.* **7**, 935–952 (2022).
15. Y. Liu *et al.*, *Nat. Biomed. Eng.* **3**, 58–68 (2019).
16. Y. S. Zhang, A. Khademhosseini, *Science* **356**, eaaf3627 (2017).
17. S. Zhang *et al.*, *Adv. Mater.* **32**, e1904752 (2020).
18. P. Li *et al.*, *Science* **384**, 557–563 (2024).
19. Y. Dai *et al.*, *Science* **386**, 431–439 (2024).
20. A. C. Tseng, T. Sakata, *ACS Appl. Mater. Interfaces* **14**, 24729–24740 (2022).
21. J. Rivnay *et al.*, *Nat. Rev. Mater.* **3**, 17086 (2018).
22. Y. Wang *et al.*, *Nat. Rev. Mater.* **9**, 249–265 (2024).
23. D. Khodagholy *et al.*, *Nat. Commun.* **4**, 2133 (2013).
24. T. Someya, Z. Bao, G. G. Malliaras, *Nature* **540**, 379–385 (2016).
25. C. Yang, Z. Suo, *Nat. Rev. Mater.* **3**, 125–142 (2018).
26. D. Nilsson *et al.*, *Adv. Mater.* **14**, 51–54 (2002).
27. D. A. Bernards, G. G. Malliaras, *Adv. Funct. Mater.* **17**, 3538–3544 (2007).
28. J. Rivnay *et al.*, *Sci. Adv.* **1**, e1400251 (2015).
29. D. Ohayon, V. Druet, S. Inal, *Chem. Soc. Rev.* **52**, 1001–1023 (2023).
30. S. Inal, J. Rivnay, A.-O. Suiu, G. G. Malliaras, I. McCulloch, *Acc. Chem. Res.* **51**, 1368–1376 (2018).
31. M. Bianchi *et al.*, *J. Mater. Chem. C* **8**, 11252–11262 (2020).
32. R. Foudazi, R. Zowada, I. Manas-Zloczower, D. L. Feke, *Langmuir* **39**, 2092–2111 (2023).
33. M. M. Michael A Leaf, *Macromolecules* **49**, 4286–4294 (2016).
34. J. Chong *et al.*, *Nat. Commun.* **14**, 2206 (2023).
35. Y. Zhu *et al.*, *ACS Appl. Mater. Interfaces* **16**, 32466–32480 (2024).
36. G. Li *et al.*, *Adv. Mater.* **34**, e2200261 (2022).
37. N. Lopez-Larrea *et al.*, *ACS Appl. Polym. Mater.* **4**, 6749–6759 (2022).
38. V. V. Tsukruk *et al.*, *Macromolecules* **30**, 6615–6625 (1997).
39. D. Liu *et al.*, *Adv. Sci. (Weinh.)* **9**, e2203418 (2022).
40. J. Rivnay *et al.*, *Adv. Mater.* **25**, 7010–7014 (2013).
41. S. Inal, G. G. Malliaras, J. Rivnay, *Nat. Commun.* **8**, 1767 (2017).
42. J. Bai *et al.*, *Sci. Adv.* **10**, eadl1856 (2024).
43. X. Tian *et al.*, *Anal. Chem.* **94**, 6156–6162 (2022).
44. D. Liu *et al.*, *Nat. Electron.* **7**, 1176–1185 (2024).
45. L. Appeltant *et al.*, *Nat. Commun.* **2**, 468 (2011).
46. M. Cucchi *et al.*, *Sci. Adv.* **7**, eabh0693 (2021).
47. X. Ji *et al.*, *Nat. Commun.* **12**, 2480 (2021).
48. X. Liang, Y. Luo, Y. Pei, M. Wang, C. Liu, *Nat. Electron.* **5**, 859–869 (2022).
49. Y. LeCun, C. Cortes, C. J. C. Burges, The MNIST database of handwritten digits (1998); https://web.archive.org/web/20200424075210/http://yann.lecun.com/exdb/mnist/index.html.
50. X. Wu *et al.*, *Nat. Commun.* **14**, 468 (2023).

ACKNOWLEDGMENTS

We thank C. Wong, J. Chan, P. S. Yip, and P. K. L. Chan from the University of Hong Kong (HKU) Central Fabrication Lab (CFL) for their support with clean-room facilities and microfabrication and the HKU Electron Microscope Unit (EMU) for assistance with morphology characterization. We also thank N. Tien and C. K. Chui for their support with printing facilities and wet lab resources at the HKU Tam Wing Fan Innovation Wing. We acknowledge N. Wong (HKU), Z. Wang (Southern University of Science and Technology), C. Li (HKU), I. McCulloch (Princeton University), H. Wang (HKU), and W. Gao (OmniVision Integrated Circuits Group, Inc.) for discussions on neuromorphic computing, molecular electronics, and the semiconductor industry. **Funding:** The Collaborative Research Fund (C7005-23Y), the Early Career Scheme (ECS) (27214224), the General Research Fund (GRF) (17208623, 17200425), and the Theme-based Research Scheme (T45-701/22-R) from the Research Grants Council of the Hong Kong SAR Government, China; the Innovation and Technology Fund (Mainland-Hong Kong Joint Funding Scheme, MHP/053/21) from the Innovation and Technology Commission (ITC) of the Hong Kong SAR Government, China; Shenzhen-Hong-Kong-Macau Technology Research Programme (SGDX20210823103537034) from the Science, Technology and Innovation Commission of Shenzhen Municipality, China; and Seed Funding for Strategic Interdisciplinary Research Scheme from HKU. **Author contributions:** Conceptualization: S.Z.; Funding acquisition: S.Z.; Supervision: S.Z.; Data curation: D.L., J.B., X.T., Y.W.; Methodology (experiment design and characterization): D.L., Y.W.; Methodology (algorithm design and simulation): D.L., X.T., J.B.; Software (miniaturized readout system): X.T., J.B.; Investigation (fabrication of hydrogel transistors): D.L., Y.W., B.C., S.D.; Investigation (sample preparation, electrochemical testing): D.L., Y.W., Z.S., C.K.L.; Investigation (cell culture and data analysis): W.L.; Formal analysis (discussion and result analysis): S.Z., G.G.M.; Writing – original draft: S.Z., D.L.; Writing – review & editing: All authors. **Competing interests:** The authors have filed a US patent on this work titled "3D semiconductor and methods of fabrication" (US application no. 63/816,028). **Data and materials availability:** All data are available in the manuscript or the supplementary materials.

SUPPLEMENTARY MATERIALS

science.org/doi/10.1126/science.adx4514
Materials and Methods; Figs. S1 to S23; Tables S1 and S2; References (*51*–*88*)

Submitted 14 March 2025; accepted 4 September 2025

10.1126/science.adx4514